

The Sunburst Arc with JWST: I. Detection of Wolf-Rayet stars injecting nitrogen into a low-metallicity, $z = 2.37$ proto-globular cluster leaking ionizing photons

T. Emil Rivera-Thorsen^{1,*}, J. Chisholm², B. Welch^{3,4,5}, J. R. Rigby⁴, T. Hutchison⁴, M. Florian⁶, K. Sharon⁷, S. Choe¹, H. Dahle⁸, M. B. Bayliss⁹, G. Khullar¹⁰, M. Gladders^{11,12}, M. Hayes¹, A. Adamo¹, M. R. Owens⁹, and K. Kim¹³

¹ The Oskar Klein Centre, Department of Astronomy, Stockholm University, AlbaNova, 10691 Stockholm, Sweden

² Department of Astronomy, University of Texas at Austin, 2515 Speedway, Austin, Texas 78712, USA

³ Department of Astronomy, University of Maryland, College Park, MD 20742, USA

⁴ Observational Cosmology Lab, Code 665, NASA Goddard Space Flight Center, 8800 Greenbelt Rd., Greenbelt, MD 20771, USA

⁵ Center for Research and Exploration in Space Science and Technology, NASA/GSFC, Greenbelt, MD 20771

⁶ Steward Observatory, University of Arizona, 933 North Cherry Avenue, Tucson, AZ 85721, USA

⁷ Department of Astronomy, University of Michigan, 1085 S. University Ave, Ann Arbor, MI 48109, USA

⁸ Institute of Theoretical Astrophysics, University of Oslo, P.O. Box 1029, Blindern, NO-0315 Oslo, Norway

⁹ Department of Physics, University of Cincinnati, Cincinnati, OH 45221, USA

¹⁰ Department of Physics and Astronomy and PITT PACC, University of Pittsburgh, Pittsburgh, PA 15260, USA

¹¹ Department of Astronomy and Astrophysics, University of Chicago, 5640 South Ellis Avenue, Chicago, IL 60637, USA

¹² Kavli Institute for Cosmological Physics, University of Chicago, Chicago, IL 60637, USA

¹³ IPAC, California Institute of Technology, 1200 E. California Blvd., Pasadena CA, 91125, USA

Received April 13., 2024; Accepted August 5., 2024.

ABSTRACT

We report the detection of a population of Wolf-Rayet (WR) stars in the Sunburst Arc, a strongly gravitationally lensed galaxy at redshift $z = 2.37$. As the brightest known lensed galaxy, the Sunburst Arc has become an important cosmic laboratory for studying star and cluster formation, Lyman α ($\text{Ly}\alpha$) radiative transfer, and Lyman Continuum (LyC) escape.

Here, we present the first results of JWST/NIRSpec IFU observations of the Sunburst Arc, focusing on a stacked spectrum of the 12-fold imaged LyC -emitting (Sunburst LCE) cluster. In agreement with previous studies, we find that the Sunburst LCE cluster is a very massive, compact star cluster with $M_{\text{dyn}} = (9 \pm 1) \times 10^6 M_{\odot}$. Our age estimate of 4.2–4.5 Myr is much larger than the crossing time of $t_{\text{cross}} = 183 \pm 9$ kyr, indicating that the cluster is dynamically evolved and consistent with being gravitationally bound. We find a significant nitrogen enhancement of the low ionization state interstellar medium (ISM), with $\log(N/O) = -0.74 \pm 0.09$, which is ≈ 0.8 dex above typical values for H II regions of similar metallicity in the local Universe. We find broad stellar emission complexes around He II $\lambda 4686$ and C IV $\lambda 5808$ with associated nitrogen emission — this is the first time WR signatures have been directly observed at redshifts above ~ 0.5 . The strength of the WR signatures cannot be reproduced by stellar population models that only include single-star evolution. While models with binary evolution better match the WR features, they still struggle to reproduce the nitrogen-enhanced WR features. JWST reveals the Sunburst LCE to be a highly ionized proto-globular cluster with low oxygen abundance and extreme nitrogen enhancement that hosts a population of Wolf-Rayet stars, likely including a previously suggested population of Very Massive Stars (VMSs), which together are rapidly enriching the surrounding medium.

Key words. Galaxies: ISM – Galaxies: evolution – Galaxies: abundances – Galaxies: star clusters: general – Stars: Wolf-Rayet

1. Introduction

Massive stars dominate the mechanical feedback, ionizing photon production, and chemical enrichment of young stellar populations. Such stars spend about $\sim 10\%$ of their lives in an evolutionary phase where they are classified as Wolf-Rayet (WR) stars (Meynet & Maeder 2005). Classical WR stars are massive, evolved, very hot stars that have lost their hydrogen envelopes (e.g., Crowder 2007). Typically, there are two formation channels to shed the outer hydrogen layers of WR stars: through extreme stellar wind mass loss (Meynet & Maeder 2005) or through close binary interactions. Metal-line absorption drives gas off the surface of massive stars; the mass-loss rate is extremely sensitive to the

metallicity of the star. Thus, though the WR phase is a fleeting part of the short life of a massive star, collectively WR stars can significantly contribute to or even dominate the winds, ionizing photons, and nucleosynthetic production of star-forming populations.

Individual WR stars have been identified out to distances of $\lesssim 5$ Mpc (e.g., Schootemeijer & Langer 2018; Della Bruna et al. 2021, 2022). WR signatures have been identified in the spectra of nearby galaxies (e.g., Vacca & Conti 1992; Gómez-González et al. 2021), and as far out as redshift $z = 0.45$ (e.g., Menacho et al. 2021; Yuan et al. 2022). WR stars are most common at higher metallicities, but WR signatures have been observed in low-metallicity galaxies (e.g., Amorín et al. 2012; Kehrig et al. 2013) and even in I Zwicky 18, the most metal-poor known galaxy

* Corresponding author. e-mail: trive@astro.su.se

(Guseva et al. 2000), demonstrating that such stripped stars are readily produced, despite the dependence of line-driven mass loss on metallicity. Binary stellar evolution paths may be particularly important at low metallicity.

Stacked rest-frame ultraviolet (UV) spectra of $z \sim 3$ galaxies have revealed broad stellar wind features that may be due to classical WR stars (Shapley et al. 2003; Rigby et al. 2018), but could also be explained by the presence of Very Massive Stars (VMSs; e.g., Wofford et al. 2014; Crowther et al. 2016; Smith et al. 2023; Upadhyaya et al. 2024). VMS are conventionally defined as main-sequence stars with $M \geq 100M_{\odot}$. Unlike lower mass main-sequence stars, VMS have strong stellar winds which make them appear spectroscopically similar to WR stars. They have not yet shed their hydrogen envelopes, so while they do display strong wind features like classical WR stars, they do not share the lacking hydrogen lines and richness in metal emission features of the latter. While the broad wind features in the rest-frame UV are almost identical for VMSs and WR stars, similar wind features exist in the rest-frame optical, which can help discriminate between the two star types (Martins et al. 2023). However, while Martins et al. present a classification scheme to distinguish between the two types of stars, Vink (2023) argues that VMSs are the same objects as the WNh type WR stars, and later evolve into classical nitrogen rich WR stars of type WN.

What has been missing, until now, is rest-frame optical spectra of the distant universe with sufficient sensitivity and dynamic range to reveal the faint, subtle signs of WR stars within their stellar populations.

In this paper, we present rest-frame optical James Webb Space Telescope (JWST)/NIRSpec Integral Field Unit (IFU) spectra of a bright, massive star cluster and surrounding H II region within the Sunburst Arc (Dahle et al. 2016), a strongly star forming galaxy at $z = 2.37$ which is gravitationally lensed by a foreground ($z = 0.44$) galaxy cluster (Sharon et al. 2022; Pignataro et al. 2021; Diego et al. 2022). The region targeted is known to be leaking ionizing photons (Rivera-Thorsen et al. 2019). By stacking the spectrum of multiple lensed images of this region, we obtain a spectrum that is directly comparable, in signal-to-noise, wavelength range, and spectral resolution, to the spectra of H II regions in the best-studied nearby galaxies. The galaxy morphology is dominated by a number of emission clumps, of which especially one is very bright (Rivera-Thorsen et al. 2019; Vanzella et al. 2022; Pignataro et al. 2021). Due to the large shear magnification, this bright clump is resolved down to pc scales, revealing a compact star cluster with a stellar population age of ~ 3.6 Myr (Chisholm et al. 2019), and steep stellar UV slope $\beta \approx -3$ (Kim et al. 2023). Chisholm et al. (2019) found broad C IV λ 1548 and H II λ 1640 stellar wind lines in rest-frame UV Magellan/MagE spectra, but it is very challenging to discriminate between the two kinds of stars from these lines alone. Pascale et al. (2023); Meštrić et al. (2023) attribute the rest-UV stellar features in the Sunburst LCE to VMSs. Pascale et al. (2023) find very strong nitrogen enhancement in hot, high-density gas condensations that they argue must be located outside, but in near proximity to, the cluster. Such very strong and highly localized nitrogen enrichment has also been observed at high redshifts since the launch of JWST, and is often, but not always, considered consistent with being injected by VMSs and WR stars (e.g., Kobayashi & Ferrara 2024; Ji et al. 2024).

2. Observations and data reduction

The target was observed with JWST/NIRCam imaging and JWST/NIRSpec integral field spectroscopy in JWST Cycle 1,

as part of program GO-2555 (PI: Rivera-Thorsen) over the time period of April 4, 2023 to April 10, 2023. The entire field was observed in each of the NIRCam filters F115W, F150W, F200W, F277W, F356W, and F444W. Four pointings were observed with NIRSpec: three on-target covering different sections of the Sunburst Arc, and one off-target for background correction (Figure 1). The target was observed in each of the settings F100L/G140H and F170L/G235H, covering a combined rest-frame wavelength range of $2900 \text{ \AA} \leq \lambda_0 \leq 9700 \text{ \AA}$; however, for the sake of this analysis, only the wavelength range $3500 \text{ \AA} \leq \lambda_0 \leq 8000 \text{ \AA}$ was used. The spectral resolving power within this wavelength interval ranges from $R \approx 2250$ ($\Delta v \approx 133 \text{ km s}^{-1}$) to $R \approx 3820$ ($\Delta v \approx 78 \text{ km s}^{-1}$) for g140h; and from $R \approx 1690$ ($\Delta v \approx 160 \text{ km s}^{-1}$), to $R \approx 3140$ ($\Delta v \approx 80 \text{ km s}^{-1}$) for g235h. The PSF of NIRSpec is not yet well characterized; but recent treatment by (D'Eugenio et al. 2023, see their Fig. 7) suggests the PSF is stable in size up to $\lambda \approx 3 \mu\text{m}$, with a minor-axis Full Width at Half Maximum FWHM $\approx 0''.1$, and a major-axis FWHM $\approx 1''.4$. For comparison, the native spaxel size of the IFU is $0''.1$.

We refer the reader to the main companion paper (Rivera-Thorsen et al., in prep.) for a thorough explanation of the data reduction and calibration steps, but outline the most important steps here. We reduced the NIRSpec IFU observations following the methods described in Rigby et al. (2023), using the TEMPLATES NIRSpec data reduction notebooks (Rigby et al. 2024). For the reduction, we used version 1.11.4 of the JWST pipeline (Bushouse et al. 2023), and the calibration reference files from context pmap_1105. After completing the pipeline reduction, we removed remaining outliers from the data cubes using the baryon-sweep software (Hutchison et al. 2024b,a).

3. Emission line modeling

We extracted a stacked spectrum from five of the six lensed images of the LCE cluster covered by the IFU (Figure 1). In the nomenclature of Rivera-Thorsen et al. (2019); Sharon et al. (2022), they are images 4, 5, 8, 9, and 10. Image 6 was partially covered by the IFU, but since the data quality was negatively affected by its position right at the edge of the detector, we omitted this image from our analysis. We extracted a spectrum from an area of 5×5 spaxels covering each image of the LCE cluster. For each spectrum, the aperture spaxels were continuum-weighted using the median value along the spectral axis before extraction. Each extracted spectrum was then normalized by the median flux value in the wavelength bins in the wavelength overlap interval between the two disperser settings. Since the spectra are differently magnified, we have made no attempt to preserve absolute fluxes, and all results in this work are based on flux ratios. The extracted spectrum displays extremely high signal-to-noise ratio and sensitivity. We detect stellar continuum at a comfortable signal-to-noise ratio across the entire wavelength range, and have identified 59 emission lines in this spectrum, including Balmer- and Paschen lines from up till level 20, as well as auroral emission lines from multiple species and ionization levels. A full analysis of abundances and ionization zones based on direct T_e methods are presented in a companion paper (Welch et al. 2024).

All subsequent line ratio based computations are based on the full flux of each line; but to account for all flux in each line as accurately as possible, we have modeled the line emission by three kinematic components, each modeled with shared FWHM and redshift, with flux in different lines left as a free parameter, such that for N emission lines with M kinematic components each included in the fit, we have a number of free parameters

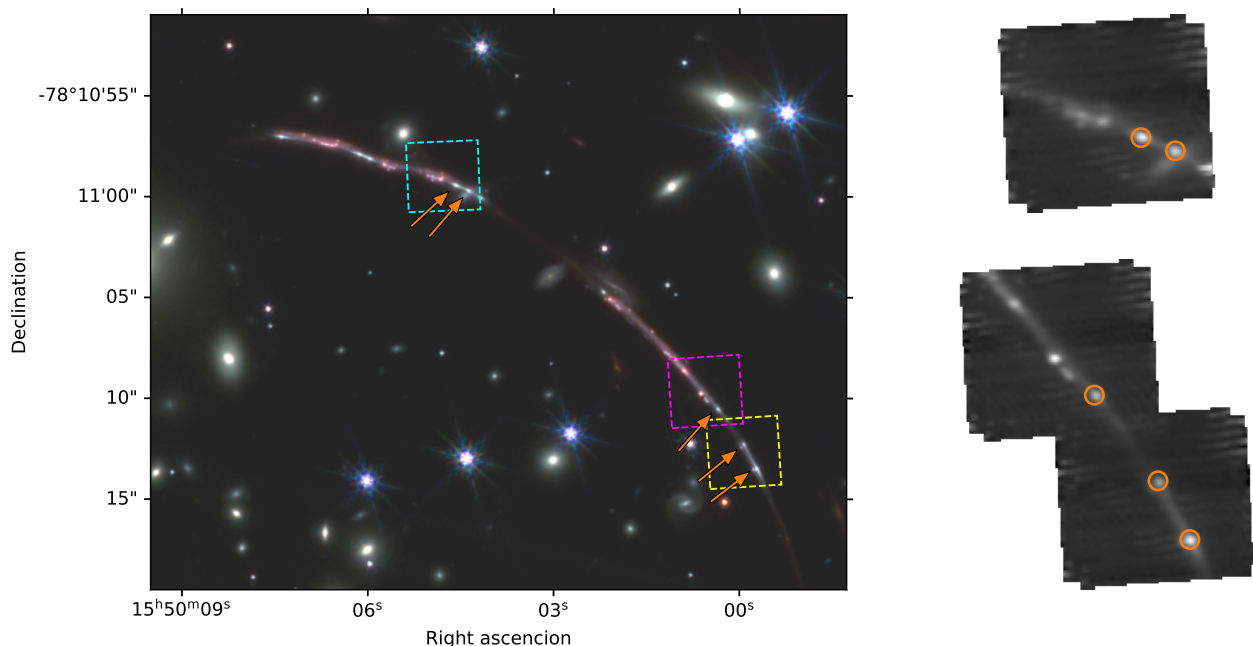


Fig. 1: Overview of the arc. **Left:** NIRCcam RGB composite of the N and NW arc segments, with R, G, B being **F444W**, **F200W**, and **F115W**, respectively, together covering the rest-frame wavelength range 3400–13000 Å. Cyan, magenta, and yellow dashed overlays show the approximate footprints of the three NIRSpect pointings 1, 2 and 3, respectively. Orange arrows show the images of the gravitationally lensed LCE cluster which were included in the stacked spectrum. **Right:** NIRSpect IFU continuum images of pointings 1 (**top right**) and combined pointings 2+3 (**bottom right**); created from a median stacking along the spectral axis of the F100L/G140H cubes. Orange circles mark the images of the LCE cluster included in the stacked spectrum.

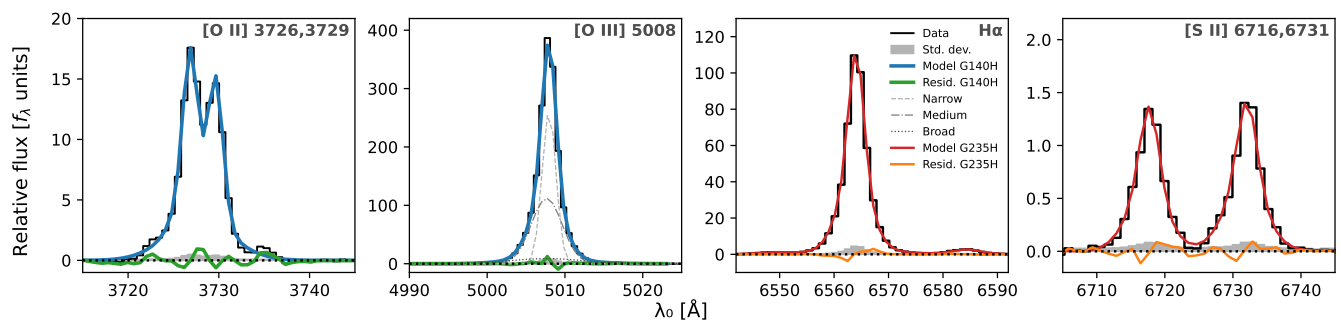


Fig. 2: Best-fit model of selected emission lines, shifted to rest-frame wavelengths. Here are shown the two strongest lines dominating the kinematics, as well as the two n_e -sensitive doublets, [O II] 3727,3729; and [S II] 6717,6731.

$n_{\text{pars}} = M(N + 2)$. In some faint lines, the broadest components have fallen below the noise level and thus only added noise to the fit, in which case they were removed. We originally included only 2 components; one narrow and one broad; but it was necessary to add a third, broad component in order to get a reasonable fit of the brightest lines, as especially H α contains a non-negligible broad component of FWHM $\approx 800 \text{ km s}^{-1}$ which likely originates from outflows driven by stellar winds from massive evolved stars in the cluster. We corrected the inferred line widths for instrument broadening using the official JWST/NIRSpect calibration files available for download at J-Docs¹ (these are the versions delivered June 2016 and are at the time of writing the most current). We interpolated the tabulated values of R , and obtained the

¹ <https://jwst-docs.stsci.edu/jwst-near-infrared-spectrograph/nirspect-instrumentation/nirspect-dispersers-and-filters>

value corresponding to the observed wavelength of each line. We assumed Gaussianity and corrected for instrument broadening by adding in quadrature the velocity dispersion and the instrument broadening in the model of each line to obtain the intrinsic line width.

Figure 2 shows a comparison of the observed data and the best-fit model for a few selected lines: [O III] 5008 and H α , which are among the lines dominating the kinematics of the fit; and the two n_e -sensitive doublets [O II] 3727,3729 and [S II] 6717,6731. Especially the [O II] doublet, which is blended at the resolving power of NIRSpect, can often have its inferred flux ratio be sensitive to an ill-fitting kinematic model. However, as is readily seen in the figure, the kinematics of the strongest lines fits well with both doublets, and we adopt the line ratios derived from these fits with good confidence.

To resolve the narrow emission to the best possible extent, we also performed a fit to the [O III] $\lambda\lambda 4960,5008$ in F100L/G140H,

where the resolving power is highest at $R \approx 3300$. This fit yielded $\text{FWHM} = 83 \text{ km s}^{-1}$, or $\sigma_{\text{LOS}} \approx 35.3 \pm 2.1 \text{ km s}^{-1}$, fully consistent with the value obtained by [Vanzella et al.](#) using VLT/X-shooter.

Table 1: best-fit kinematic properties of the three components.

Comp.	z	Δv^a	FWHM^a
Narrow ^b	$2.371062 \pm 6 \times 10^{-6}$	—	91 ± 7
Medium	$2.37093 \pm 2 \times 10^{-5}$	-11.7 ± 1.9	277 ± 6
Broad	$2.3709 \pm 2 \times 10^{-4}$	-14.4 ± 17.8	708 ± 22

Notes.

^(a) Given in km s^{-1} relative to the narrow component.

^(b) The best-fit narrow component FWHM from [O III] in G140H is $83 \pm 4.9 \text{ km s}^{-1}$

Table 2: Measured line fluxes relative to H β .

Line	Relative flux [%]	Uncertainty [%]
[O II] 3727	30.66	5.31
[O II] 3729	22.87	5.91
[O III] 4363	10.94	6.07
H β 4861	100	—
[O III] 4960	237.58	19.15
[O III] 5008	707.32	56.67
H α 6562	334.17	27.59
[N II] 6548	4.81	0.79
[N II] 6584	11.07	1.18
[S II] 6717	4.20	0.52
[S II] 6731	4.47	0.53

Tables 1 and 2 show the results of the modeling; the former shows the centroid and line widths of the three kinematic components, while the latter shows the total measured flux of the measured lines relative to the measured flux in H β .

4. LCE Cluster properties

4.1. Detection of Wolf-Rayet Stars

Previous ground-based, rest-frame UV spectroscopic observations with Magellan and the VLT have shown broad stellar emission in He II λ 1640 and C IV λ 1548 ([Chisholm et al. 2019](#); [Meštrić et al. 2023](#)). These lines are typically attributed to Wolf-Rayet stars, but can also be attributed to VMSs; usually defined as main sequence stars of $M_{\star} \geq 100 M_{\odot}$. The emission has been attributed to VMSs by, e.g., [Meštrić et al. \(2023\)](#) and [Pascale et al. \(2023\)](#) from secondary evidence; but it is very difficult to distinguish these two scenarios from the rest-frame UV emission alone. This degeneracy can, however, be broken with rest-frame optical spectral features. The classical Wolf-Rayet “bumps” at $\sim 4686 \text{ \AA}$ (the “blue bump”) and $\sim 5808 \text{ \AA}$ (the “yellow”, “orange” or sometimes “red bump”); here we adopt the term “orange”) consist of complexes of metal lines centered around He II λ 4686 (blue) and C IV λ 5808 (orange), which are present at varying strengths depending on the metal abundances, ionization/temperature, and

other properties of the stars from which they originate. This allows for a distinction between VMS and WR stars, as outlined in the classification scheme by [Martins et al. \(2023\)](#). According to this scheme, VMS give rise to a blue bump dominated by stellar He II, and the orange bump, if present at all, is weak and consisting of a simple C IV doublet; the dense complex of surrounding metal lines is largely absent.

[Figure 3](#) shows the stacked spectrum of the Sunburst LCE cluster in the relevant wavelength intervals. The spectrum shows a clear, broad blue bump, and a somewhat weaker broad orange bump. The two features are shown in close-up in the lower panels. Two forbidden, nebular Argon lines [Ar IV] $\lambda\lambda$ 4711, 4740 coincide with the red side of the blue bump, but are not part of this line complex; neither is the narrow, nebular He I λ 5875 line.

To measure line width and flux of the WR He II 4686 feature, we have fit it a single Gaussian profile. We have enforced the continuum level shown in the upper panel, and included the wavelength interval between [Fe III] and [Ar IV] only. The fit yields a velocity FWHM = $1370 \pm 250 \text{ km s}^{-1}$ and restframe EW = $4.1 \pm 0.4 \text{ \AA}$. Following the methodology of [Martins et al.](#), the widths and relative strengths of the bumps, and in particular the prevalence of the permitted N III features at $\lambda\lambda$ 4620, 4640, all place these features firmly in the Wolf-Rayet category. However, since what separates the two stellar types in this scheme is mainly the absence of certain features in VMS compared to WR stars, having found strong spectroscopic evidence for WR stars does not rule out a — potentially significant — contribution from VMS; see [Sect. 4.6](#).

4.2. Dust attenuation

To model dust attenuation, we have adopted a standard starburst attenuation law ([Calzetti et al. 2000](#)) with a standard value of $R_V \equiv A_V/E(B-V) = 4.05$. We have computed $E(B-V)$ following [Calzetti et al. \(2000\)](#). Adopting a standard intrinsic $H\alpha/H\beta = 2.86$ yields a value of $E(B-V) = 0.11 \pm 0.19$, which we have adopted to deredden line fluxes.

4.3. Dynamical mass

Following [Rhoads et al. \(2014\)](#); [Vanzella et al. \(2022\)](#); we find the dynamical mass using the approximation $M_{\text{Dyn}} \approx 4\sigma_{\text{LOS}}^2 R_{\text{eff}}/G$; with R_{eff} being the effective radius of the LCE cluster. Since we do not have a measurement of the stellar velocity dispersion, we have adopted the line width of the narrow component of the strong emission lines H α , H β , and the [O III] doublet at 4960, 5008 \AA as a proxy for $\sigma_{\text{LOS}} = 38.6 \pm 2.9 \text{ km s}^{-1}$. Adopting the value $R_{\text{eff}} = 7.8 \text{ pc}$ ([Meštrić et al. 2023](#)), we find $M_{\text{dyn}} = (9.0 \pm 1.1) \times 10^6 M_{\odot}$.

4.4. Oxygen abundance

We have estimated the oxygen abundance in the gas based on the direct T_e method, following the recipe of [Pérez-Montero \(2017\)](#), using the O⁺ and O⁺⁺ based abundances together; we have not observed any nebular He II and thus believe the contribution of higher ionization stages is negligible.

We have first found electron temperature and density using PYNEB ([Luridiana et al. 2015](#)) and its getCrossTemDen method, which yielded $T_e = 14 \pm 3 \text{ kK}$ and $n_e(\text{O}^+) = 1440_{-870}^{+1360} \text{ cm}^{-3}$. Using [S II] $\lambda\lambda$ 6716, 6731 as an n_e diagnostic instead yields an identical value of T_e , and an electron density of $n_e(\text{S}^+) = 1040_{-490}^{+620} \text{ cm}^{-3}$.

Following eqs. 38 and 40 in [Pérez-Montero \(2017\)](#), we find:

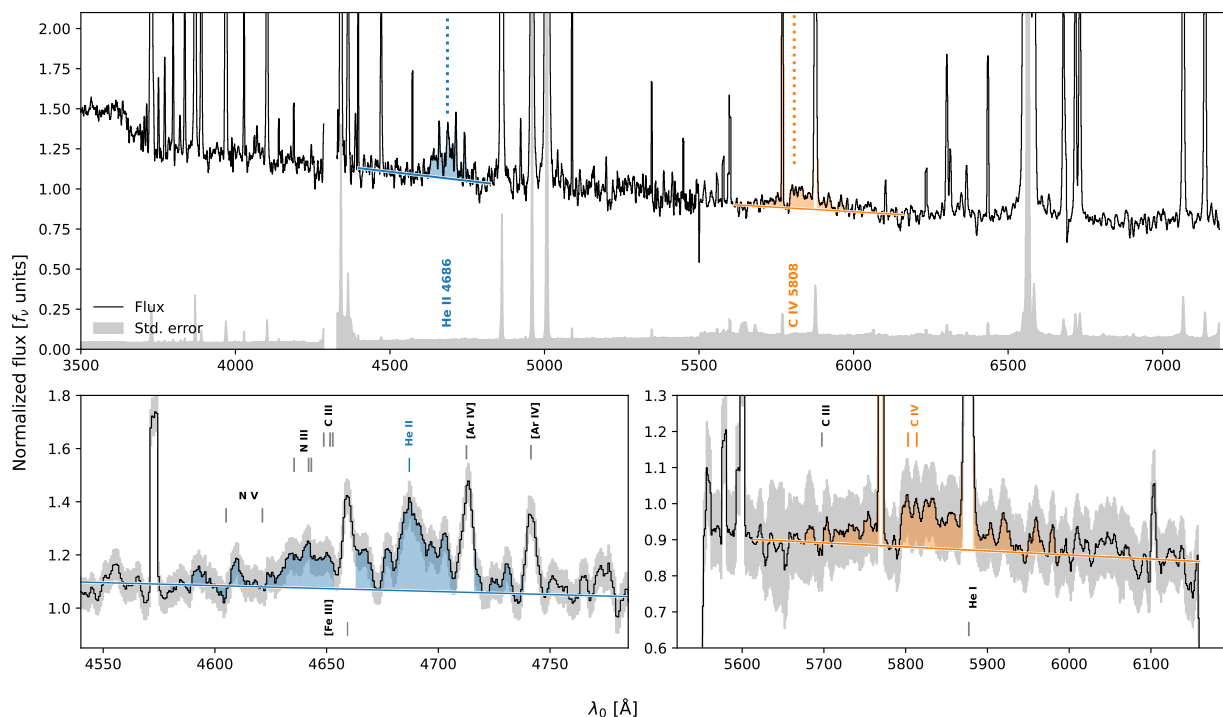


Fig. 3: Extracted and stacked spectrum of the Sunburst LCE, zoomed into the continuum to clearly show the blue and orange WR bumps. Blueward of 5500 Å, only the G140H spectrum is shown; redward, only the G235H spectrum is shown. Almost all the spikes are emission lines. The best-fit continuum at each bump is shown in its corresponding color. Lower left: Detailed view of the blue WR bump; the gray shading shows the $\pm 1\sigma$ errors. A number of emission line centroids are marked. Lower right: A similar detailed view of the orange WR bump, centered on the C IV $\lambda\lambda$ 5801,5812 Å feature. On its red side is a He I λ 5875 emission line; on the blue side an instrument artifact. The blue and orange shading of the bumps is mainly provided to guide the eye.

$$12 + \log\left(\frac{\text{O}^+}{\text{H}^+}\right) = 6.65^{+0.39}_{-0.27}; \quad 12 + \log\left(\frac{\text{O}^{2+}}{\text{H}^+}\right) = 7.95^{+0.32}_{-0.22}$$

and from the approximation $\text{O}/\text{H} = (\text{O}^+ + \text{O}^{2+})/\text{H}^+$ (Izotov et al. 2006; Pérez-Montero 2017), we get $12 + \log(\text{O}/\text{H}) = 7.97^{+0.33}_{-0.21}$.

Adopting the solar value of $12 + \log(\text{O}/\text{H}) = 8.69$ from Asplund et al. (2009), this yields an oxygen abundance for the sunburst LCE cluster gas of about $0.19^{+0.20}_{-0.07} Z_{\odot}$. Chisholm et al. (2019) found a stellar metallicity of $Z_{\star} \approx 0.3 Z_{\odot}$ and Pascale et al. (2023) found a nebular metallicity of $Z_{\text{neb}} \approx 0.26 Z_{\odot}$ — both higher than the nebular abundance found in this work, but fully consistent within the error bars. From the derived temperature and density, we have also derived the pressure, and found $P_{\text{ion}}/k_B = (3.6^{+2.6}_{-1.6}) \times 10^7 \text{ K cm}^{-3}$. This is consistent with values in the centers of local Universe starburst galaxies (Della Bruna et al. 2021, 2022).

4.5. Nitrogen enhancement

Despite having low metallicity, the Sunburst LCE cluster is highly nitrogen enriched. Pascale et al. (2023) report $\log(\text{N}/\text{O}) = -0.23^{+0.08}_{-0.11}$ based on rest-frame UV N III] emission from VLT/X-shooter spectroscopy.

Here, we have computed $\log(\text{N}/\text{O})$ from [O II] $\lambda\lambda$ 3727,3729 and [N II] λ 6584 following Pérez-Montero (2017). This ion abundance ratio is expected to follow the true element abundance closely because of the strong similarity in ionization potentials between the two species. Still following Pérez-Montero (2017), we computed

$$t([\text{N II}]) \equiv 10^{-4} T_e(\text{N}^+) = \frac{1.85}{[t([\text{O III}] - 0.72)]}$$

and adopted this as the low-excitation temperature in the nomenclature of those authors². We derive an [N II] -based nitrogen abundance for the Sunburst LCE of $\log(\text{N}/\text{O}) = -0.74 \pm 0.09$. This value is ~ 0.7 (Berg et al. 2012) to 0.8 (Topping et al. 2024) dex above the typical value for local Universe H II regions with the same oxygen abundance $12 + \log(\text{O}/\text{H}) \approx 7.95$; but still half a dex below the even higher N III] based value found by Pascale et al. (2023). We find that this corroborates the hypothesis put forward by Pascale et al., that the majority of the nitrogen enhancement in the Sunburst LCE is found in dense, highly ionized clouds in close vicinity of the LCE cluster, the most massive members of which are currently the main drivers of this nitrogen enhancement. A similar scenario has also been suggested recently for high-redshift galaxies in general by Ji et al. (2024), who also suggest that the surrounding, low-density gas has a more normal chemical evolution.

Recent observations of galaxies at $z > 10$ have found extreme N/O enhancements only a few 100 Myr after the Big Bang that has been compared to the Sunburst Arc (Cameron et al. 2023; Senchyna et al. 2023; Marques-Chaves et al. 2024; Castellano et al. 2024). Nitrogen is often thought to be produced by long-lived evolved lower mass stars, and these extreme N/O observations in the early universe have questioned the origin of early nitrogen production. The observations of WR stars within the

² Adopting the [O III] λ 4363 -based value of T_e only changed the end result marginally.

Sunburst Arc point to a plausible causal origin of the nitrogen: extreme nitrogen production from classical WR and WNh stars (Berg et al. 2012; Kobayashi & Ferrara 2024). This suggests that short-lived evolved massive stars may play a crucial role in the build-up of metals within the first few 100 Myr of cosmic history and might hold a key to inferring the properties of the first galaxies formed in the universe.

In this work, we find that while the nitrogen enhancement in the low-density medium is far lower than in the denser medium, it is still quite strongly enhanced.

This also challenges one part of the scenario proposed by Pascale et al.: that the dense, ionized medium is located outside and at a distance from the LCE cluster. Such a scenario would see a higher Nitrogen abundance in the neutral, low-density medium compared to the dense medium than we observe here. Rather, this gas might be dense condensations within the LCE cluster itself, in close proximity to the most massive stars.

4.6. WR population properties

To investigate the properties of the WR population, we have compared the WR bumps to synthetic spectra produced by the BPASS code (Eldridge et al. 2017; Stanway & Eldridge 2018; Stevance et al. 2020), see Figure 4. These spectra were taken from the “fiducial” suite of models, produced using a Kroupa IMF with slope of -2.35 , minimum and maximum stellar masses of 0.5 , $300 M_{\odot}$, and a metallicity of $Z = 0.04 \approx 20\% Z_{\odot}$ (Stevance et al. 2020). For each time step, we show the synthetic spectrum with binary evolution tracks enabled (leftmost panels), and disabled (rightmost panels).

Following the method outlined by del Valle-Espinosa et al. (2023), we have visually compared BPASS age steps in the range $6.3 \leq \log(\text{age [yrs]}) \leq 6.8$, during which WR stars are prevalent, to the observed spectrum. In particular, we have looked for the age step at which the relative strengths of the two emission features is best emulated by the model spectra. Using the relative heights of the bumps as a proxy for their relative fluxes, we found that the observed spectra had a peak ratio between the bumps of $I(4686)/I(5808)_{\text{obs}} \approx 2.35$. The model spectrum yielded $I(4686)/I(5808) \approx 1.79$ at 4 Myr burst age, and $I(4686)/I(5808) \approx 8.24$ at 5 Myr burst age. The observed spectrum is sandwiched between these two ages, but closer to 4 Myr than 5 Myr of age. For comparison, Chisholm et al. (2019) found a light-weighted cluster age of 3.6 Myr from fitting a similar class of BPASS models to stacked, rest-frame UV slit spectra of the Sunburst LCE. The difference of ~ 0.5 Myr is not significant, as on these short timescales the assumption of an instantaneous starburst likely breaks down.

The best fitting BPASS model population corresponding to 19% solar metallicity and a population age of 4 Myr contains (adjusted for mass) ~ 900 WR stars, with the fractions of WNh, WN, and WC stars being 68%, 19%, and 13%, respectively. Assuming that VMS are indeed WNh stars later evolving into classical WN stars as suggested by Vink (2023), we may be looking at a snapshot of just such an evolutionary sequence.

We tested BPASS models of other metallicities within the confidence interval of the computed values. We found that the WR models favor lower metallicities, around $10\% Z_{\odot}$, in which case a slightly larger age ~ 5 Myr is favored; and that the WR peaks are inconsistent with anything higher than $25\% Z_{\odot}$. We note that the observed WR bumps are brighter relative to the underlying continuum than the model spectrum from BPASS. This could in theory be due to stronger winds in the WR stars, but these winds are line driven and are weak at low metallicity. As is

visible from Figure 4, a binary population is needed to account for the observed WR emission strength, to compensate for the weaker wind stripping. Adamo et al. (2024) show in their figure 2 an overview of inferred surface density and effective radius for a population of star clusters, including the Sunburst LCE. These authors find that the cluster is consistent with being a very massive proto-globular cluster with a high stellar density. This could statistically lead to an enhanced fraction of binary systems and in turn an enhanced VMS and/or WR population. Alternatively, a more top-heavy IMF than adopted in the fiducial BPASS models could also give rise to a larger population of WR stars.

We also note that the WR bumps of the Sunburst LCE are much broader than those of the model spectra. While the model spectra at these metallicities are clearly dominated by He II and C IV, the observed bumps also show rich emission in the adjacent metal line complexes, in particular in N III around 4650 \AA . This shows significant nitrogen enhancement in the evolved massive stars of the cluster; consistent with the suggestion by Kobayashi & Ferrara (2024) that evolved, massive stars drive rapid nitrogen enhancement in the early phases of cluster evolution.

4.7. The relative contributions from VMS and classic WR stars

As previously stated, other authors have attributed the rest-frame UV stellar wind features to Very Massive Stars, based on the observation from low-redshift galaxies that the fraction of WR stars at low stellar metallicity is very low (e.g., Crowther & Hadfield 2006; Crowther et al. 2023). Mayya et al. (2023) have studied the star forming ring of the Cartwheel galaxy, which has a metallicity similar to that of the Sunburst LCE cluster. In this study, they calculated that the He II bump would have an $EW > 2 \text{ \AA}$ only when a contingent of VMS was present. Our own comparison to the fiducial BPASS models in Sect. 4.6 suggests that a fraction of $\sim 70\%$ WNh stars/VMS best simultaneously reproduces the combined Blue Bump equivalent width and bump intensity ratio, supporting that a large population of VMS is present. In contrast to this stands the morphology of the bumps, and especially the strength of the surrounding metal lines, primarily [N III]. The BPASS models fail to reproduce the bump morphology and the metal line strength at this metallicity, as is evident in Figure 4. Also the Martins et al. (2023) morphological classification scheme of the Blue and Orange bumps firmly classifies these bumps as stemming from classical WR stars. The Martins et al. (2023) scheme is demonstrated and developed in the context of a galaxy of somewhat higher metallicity than the Sunburst LCE; however, the spectral features of the individual classes of VMS/WR stars are not expected to change with metallicity, only the overall and relative numbers of these star types. Given that the stellar wind features of VMS/WNh are a subset of those of classical WR stars, the Martins et al. (2023) scheme cannot rule out a contribution from VMS; only suggest that it is considerably less dominant than in the BPASS models.

Additionally, regardless of the relative contributions from VMS and classic WR stars, it is clear that the fiducial BPASS model cannot reproduce the strength of the Blue and Orange bumps. It is necessary to invoke some mechanism or mechanisms which would give rise to a larger number of classic, hydrogen-stripped WR stars than this model; and in the previous section we suggested a higher binary fraction among the massive stars, due to the dense environment in this cluster. Such a boost to binary evolution could boost the population of classical WR stars

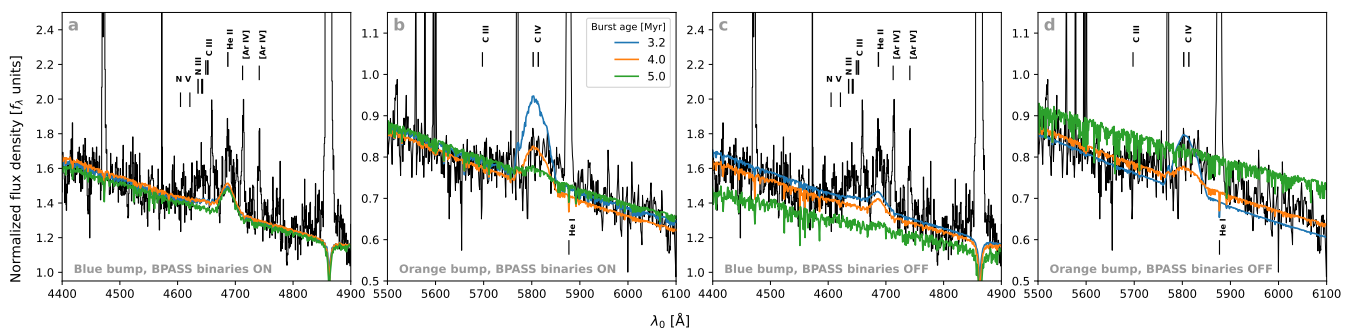


Fig. 4: The blue (a, c) and orange (b, d) WR bumps in the Sunburst LCE, this time shown in normalized f_λ units. Along with the observed data is shown a selection of the fiducial BPASS (Eldridge et al. 2017; Stanway & Eldridge 2018; Stevance et al. 2020) synthetic spectra corresponding to a metallicity of 19% Z_\odot as found from the direct method, and the range of ages at which a considerable WR population can be present. The models in panels a and b have binary evolution enabled, in panels c and d they are disabled.

considerably, and it could then lead one to ask whether invoking a VMS contribution would still be necessary to explain the bumps.

Clearly, closer analysis and higher signal-to-noise data would be necessary to properly settle this question; but tentatively, we can say with confidence that a surprisingly strong classic WR population is necessary to account for the observed bump morphologies, that a considerable contribution from VMS seems plausible but more difficult to ascertain, and that it seems likely that the 70% VMS predicted by the fiducial BPASS model probably is an overestimate due to its failure to reproduce the broad metal emission features observed.

4.8. Age from $EW(H\alpha)$

These NIRSpect IFU spectra, covering the rest-frame optical in the Sunburst Arc, are the first detection of rest-frame optical continuum in this galaxy; allowing the first spectroscopic measurement of the equivalent width of $H\alpha$, $EW_0(H\alpha) = 1040 \pm 31 \text{ \AA}$. Given that the Sunburst LCE cluster is leaking ionizing radiation, this value should be corrected for the amount of ionizing photons that have not been reabsorbed in the ISM giving rise to recombination lines. However, although the line-of-sight ionizing escape fraction is high (Rivera-Thorsen et al. 2019); Rivera-Thorsen et al. (2017) have argued based on the properties of $Ly\alpha$ that the global escape fraction is much lower than that, perhaps as low as $2\% \lesssim f_{\text{esc, glob}}^{\text{LyC}} \lesssim 5\%$.

Comparing to STARBURST 99 models for the relevant metallicity³ shows that the uncorrected $EW(H\alpha)$ is consistent with a cluster age of $\log(\text{age [yrs]}) \sim 6.6$ or just under 4 Myr; within the same logarithmic age step best matching the WR emission. A more in-depth comparison of the age constraints imposed by $H\alpha$ and WR emission could potentially help constrain the global LyC escape fraction, and test the $Ly\alpha$ radiative transfer and ISM geometry scenario put forward by Rivera-Thorsen et al. (2017).

5. Summary and conclusion

1. The Sunburst LCE cluster has a dynamical mass of $(9.0 \pm 1.1) \times 10^6 M_\odot$. Accounting for typical mass loss over the age of local GCs (e.g., Adamo et al. 2024), this brings the mass of the Sunburst LCE cluster very close to e.g., ω Cen.

³ https://www.stsci.edu/science/starburst99/figs/wha_inst_d.html

Table 3: Derived physical properties of the Sunburst LCE cluster.

Property	Value
z_{LCE}^a	$2.37108 \pm 2 \times 10^{-5}$
$E(B - V)_{H\alpha/H\beta}$	0.11 ± 0.19
$EW_0(H\alpha) [\text{\AA}]$	1040 ± 31
Dynamical mass [$10^6 M_\odot$]	9.0 ± 2.7
T_e ([O III]) [$10^4 K$]	1.4 ± 0.3
T_e ([N II]) [$10^4 K$]	1.34×10^4
n_e ([O II]) [cm^{-2}]	1400_{-800}^{+1500}
n_e ([S II]) [cm^{-2}]	1000_{-400}^{+600}
P_{ion}/k_B [$10^7 K/\text{cm}^3$]	$3.6_{-1.6}^{+2.6}$
$12 + \log(\text{O}/\text{H})$ ($\text{O}^+ + \text{O}^{++}$)	$7.96_{-0.21}^{+0.33}$
$\log(\text{N}/\text{O})$	-0.74 ± 0.09

Notes. ^(a) Based on the full set of emission lines in G140H.

2. The Sunburst LCE cluster has a moderately low oxygen abundance of $12 + \log(\text{O}/\text{H}) = 7.96_{-0.21}^{+0.33}$, or just under 20% Z_\odot , but an N/O ratio in the low-ionized medium slightly above solar.
3. The LCE cluster contains a population of massive Wolf-Rayet stars; to our knowledge, this is the first time these have been directly and unambiguously identified using the rest-frame optical WR features at $z \gtrsim 0.5$. The relative strengths of the blue and the orange WR bumps, compared to BPASS synthetic spectra, sets the LCE cluster age to slightly above 4 Myr. Adopting the numbers from the BPASS model and scaling for cluster mass, assuming that the dynamical mass is entirely stellar, yields a total of ~ 700 WR stars in the LCE cluster.
4. The BPASS model best fitting the blue-to-orange bump ratio contains as many as $\sim 70\%$ WNh stars, which are generally accepted as a spectroscopic designation of VMS. However, while these models can reproduce the relative bump strength well, they fail to reproduce the broad metal emission features surrounding the main He II and C III features. It is unclear whether the rapid nitrogen enrichment modeled by Vink (2023); Kobayashi & Ferrara (2024) can account for this discrepancy, but we tentatively suggest that the VMS/WR ratio predicted by the best BPASS model might be too high.

5. The BPASS models with no binary evolution included produced a much poorer approximation to the observed spectra than those with binary evolution enabled. In particular, they all fail to produce a blue/orange ratio larger than 1.
6. The observed WR bump strength relative to the underlying continuum is stronger than in any of the model spectra, indicating that the Sunburst LCE cluster contains more, or more luminous, WR stars than assumed in the models. A number of possible explanations could conceivably account for this, e.g., a more top-heavy IMF, enhanced binary fraction, or stronger winds driven by rapid nitrogen enrichment. These data provide key observational constraints on stellar population models such as BPASS.
7. The LCE cluster is markedly nitrogen enriched for its low metallicity, with $\log(N/O) = -0.74 \pm 0.09$; about 0.8 dex higher than typical values for known H II regions of similar metallicity at low redshifts. The even higher $\log(N/O) = -0.2$ in the dense, ionized condensations reported by Pascale et al. (2023) suggests that the majority of the nitrogen sits in compact, highly ionized gas close to the most massive stars. This in turn lends credence to the hypothesis that we are observing a rapid, ongoing nitrogen enrichment of the cluster, driven mainly by very massive and bright stars, and lends credence to the hypothesis by Ji et al. (2024) that most of the rapid nitrogen enrichment seen in galaxies such as gn-z11 is concentrated in high density and high-ionization regions around evolved high-mass stars, while the low-pressure and low-ionization evolves more moderately.

These hints together show a picture of a proto-globular cluster at roughly 20% the current age of the Universe with a bright population of Wolf-Rayet stars, likely along with a significant contingent of Very Massive Stars, rapidly injecting nitrogen and other heavier elements into its ISM. The large WR star and VMS population indicates a generally large population of massive stars, possibly combined with a high binarity fraction, leading to a stronger and perhaps more protracted production of ionizing photons than accounted for by the models.

Acknowledgements. The authors want to thank A. Bik, A. Saldana-Lopez, and M. del Valle-Espinosa for helpful comments and suggestions. This work is based on observations made with the NASA/ESA/CSA James Webb Space Telescope. The data were obtained from the Mikulski Archive for Space Telescopes at the Space Telescope Science Institute, which is operated by the Association of Universities for Research in Astronomy, Inc., under NASA contract NAS 5-03127 for JWST. These observations are associated with program GO 2555. Support for program #2555 was provided by NASA through a grant from the Space Telescope Science Institute, which is operated by the Association of Universities for Research in Astronomy, Inc., under NASA contract NAS 5-03127. ER-T is supported by the Swedish Research Council grant No. 2022-04805_VR.

References

- Adamo, A., Bradley, L. D., Vanzella, E., et al. 2024, arXiv e-prints, arXiv:2401.03224
- Amorín, R. O., Vílchez, J. M., & Pérez-Montero, E. 2012, Unveiling the Nature of the "Green Pea" Galaxies, ed. P. Papaderos, S. Recchi, & G. Hensler, 243
- Asplund, M., Grevesse, N., Sauval, A. J., & Scott, P. 2009, ARA&A, 47, 481
- Berg, D. A., Skillman, E. D., Marble, A. R., et al. 2012, ApJ, 754, 98
- Bushouse, H., Eisenhamer, J., Dencheva, N., et al. 2023, JWST Calibration Pipeline
- Calzetti, D., Armus, L., Bohlin, R. C., et al. 2000, ApJ, 533, 682
- Cameron, A. J., Katz, H., Rey, M. P., & Saxena, A. 2023, MNRAS, 523, 3516
- Castellano, M., Napolitano, L., Fontana, A., et al. 2024, arXiv e-prints, arXiv:2403.10238
- Chisholm, J., Rigby, J. R., Bayliss, M., et al. 2019, ApJ, 882, 182
- Crowther, P. A. 2007, ARA&A, 45, 177
- Crowther, P. A., Caballero-Nieves, S. M., Bostroem, K. A., et al. 2016, MNRAS, 458, 624
- Crowther, P. A. & Hadfield, L. J. 2006, A&A, 449, 711
- Crowther, P. A., Rate, G., & Bestenlehner, J. M. 2023, MNRAS, 521, 585
- Dahle, H., Aghanim, N., Guennou, L., et al. 2016, A&A, 590, L4
- del Valle-Espinosa, M. G., Sánchez-Janssen, R., Amorín, R., et al. 2023, MNRAS, 522, 2089
- Della Bruna, L., Adamo, A., Lee, J. C., et al. 2021, A&A, 650, A103
- Della Bruna, L., Adamo, A., McLeod, A. F., et al. 2022, A&A, 666, A29
- D'Eugenio, F., Perez-Gonzalez, P., Maiolino, R., et al. 2023, arXiv e-prints, arXiv:2308.06317
- Diego, J. M., Pascale, M., Kavanagh, B. J., et al. 2022, A&A, 665, A134
- Eldridge, J. J., Stanway, E. R., Xiao, L., et al. 2017, PASA, 34, e058
- Gómez-González, V. M. A., Mayya, Y. D., Toalá, J. A., et al. 2021, MNRAS, 500, 2076
- Guseva, N. G., Izotov, Y. I., & Thuan, T. X. 2000, ApJ, 531, 776
- Hutchison, T. A., Welch, B. D., Rigby, J. R., et al. 2024a, baryon-sweep: Outlier rejection algorithm for JWST/NIRSpec IFS data, Astrophysics Source Code Library, record ascl:2401.012
- Hutchison, T. A., Welch, B. D., Rigby, J. R., et al. 2024b, PASP, 136, 044503
- Izotov, Y. I., Stasińska, G., Meynet, G., Guseva, N. G., & Thuan, T. X. 2006, A&A, 448, 955
- Ji, X., Übler, H., Maiolino, R., et al. 2024, arXiv e-prints, arXiv:2404.04148
- Kehrig, C., Pérez-Montero, E., Vílchez, J. M., et al. 2013, MNRAS, 432, 2731
- Kim, K. J., Bayliss, M. B., Rigby, J. R., et al. 2023, ApJ, 955, L17
- Kobayashi, C. & Ferrara, A. 2024, ApJ, 962, L6
- Luridiana, V., Morisset, C., & Shaw, R. A. 2015, A&A, 573, A42
- Marques-Chaves, R., Schaerer, D., Kuruvanthodi, A., et al. 2024, A&A, 681, A30
- Martins, F., Schaerer, D., Marques-Chaves, R., & Upadhyaya, A. 2023, A&A, 678, A159
- Mayya, Y. D., Plat, A., Gómez-González, V. M. A., et al. 2023, MNRAS, 519, 5492
- Menacho, V., Östlin, G., Bik, A., et al. 2021, MNRAS, 506, 1777
- Meštrić, U., Vanzella, E., Upadhyaya, A., et al. 2023, A&A, 673, A50
- Meynet, G. & Maeder, A. 2005, A&A, 429, 581
- Pascale, M., Dai, L., McKee, C. F., & Tsang, B. T. H. 2023, ApJ, 957, 77
- Pérez-Montero, E. 2017, PASP, 129, 043001
- Pignataro, G. V., Bergamini, P., Meneghetti, M., et al. 2021, A&A, 655, A81
- Rhoads, J. E., Malhotra, S., Richardson, M. L. A., et al. 2014, ApJ, 780, 20
- Rigby, J., Hutchison, T. A., Rivera-Thorsen, T. E., et al. 2024, JWST-Templates/Notebooks: minor update, added DOI tracker
- Rigby, J. R., Bayliss, M. B., Chisholm, J., et al. 2018, ApJ, 853, 87
- Rigby, J. R., Vieira, J. D., Phadke, K. A., et al. 2023, arXiv e-prints, arXiv:2312.10465
- Rivera-Thorsen, T. E., Dahle, H., Chisholm, J., et al. 2019, Science, 366, 738
- Rivera-Thorsen, T. E., Dahle, H., Gronke, M., et al. 2017, A&A, 608, L4
- Schootemeijer, A. & Langer, N. 2018, A&A, 611, A75
- Senchyna, P., Plat, A., Stark, D. P., & Rudie, G. C. 2023, arXiv e-prints, arXiv:2303.04179
- Shapley, A. E., Steidel, C. C., Pettini, M., & Adelberger, K. L. 2003, ApJ, 588, 65
- Sharon, K., Mahler, G., Rivera-Thorsen, T. E., et al. 2022, ApJ, 941, 203
- Smith, L. J., Oey, M. S., Hernandez, S., et al. 2023, ApJ, 958, 194
- Stanway, E. R. & Eldridge, J. J. 2018, MNRAS, 479, 75
- Stevance, H., Eldridge, J., & Stanway, E. 2020, The Journal of Open Source Software, 5, 1987
- Topping, M. W., Stark, D. P., Senchyna, P., et al. 2024, MNRAS, 529, 3301
- Upadhyaya, A., Marques-Chaves, R., Schaerer, D., et al. 2024, A&A, 686, A185
- Vacca, W. D. & Conti, P. S. 1992, ApJ, 401, 543
- Vanzella, E., Castellano, M., Bergamini, P., et al. 2022, A&A, 659, A2
- Vink, J. S. 2023, A&A, 679, L9
- Welch, B., Rivera-Thorsen, T. E., Rigby, J., et al. 2024, arXiv e-prints, arXiv:2405.06631
- Wofford, A., Leitherer, C., Chandar, R., & Bouret, J.-C. 2014, ApJ, 781, 122
- Yuan, A., Yang, C., Zhong, G., et al. 2022, MNRAS, 510, 309